Soft Matter

# Hysteresis in spreading and retraction of liquid droplets on parallel fiber rails



| | |
|---|---|
| Journal: | *Soft Matter* |
| Manuscript ID | SM-ART-01-2021-000126.R1 |
| Article Type: | Paper |
| Date Submitted by the Author: | 03-Apr-2021 |
| Complete List of Authors: | Wang, Fang; Clemson University, Department of Materials Science and Engineering<br>Schiller, Ulf; Clemson University, Department of Materials Science and Engineering |
| | |

Soft Matter

ARTICLE TYPE

Cite this: DOI: 00.0000/xxxxxxxxxx

# Hysteresis in spreading and retraction of liquid droplets on parallel fiber rails†

Fang Wang[a] and Ulf D. Schiller*[a]

Received Date
Accepted Date

DOI: 00.0000/xxxxxxxxxx

Wetting and spreading of liquids on fibers occurs in many natural and artificial processes. Unlike on a planar substrate, a droplet attached to one or more fibers can assume several different shapes depending on geometrical parameters such as liquid volume and fiber size and distance. This paper presents lattice Boltzmann simulations of the morphology of liquid droplets on two parallel cylindrical fibers. We investigate the final shapes resulting from spreading of an initially spherical droplet deposited on the fibers and from retraction of an initial liquid column deposited between the fibers. We observe three possible equilibrium configurations: barrel-shaped droplet, droplet bridges, and liquid columns. We determine the complete morphology diagram for varying inter-fiber spacing and liquid volume and find a region of bistability that spans both the column regime and the droplet regime. We further present a simulation protocol that allows to probe the hysteresis of transitions between different shapes. The results provide insights into energies and forces associated with shape transformations of droplets on fibers that can be used to develop fiber-based materials and microfluidic systems for manipulation of liquids at small scale.

## 1 Introduction

Liquid-fiber interactions play an important role in many natural and engineered processes including wetting and drying of hair or feathers[1,2], wicking of fabrics[3], coalescence filtration[4], and fiber coating[5]. Advances in fabrication of functional fibers also make it possible to use droplet-fiber system as building blocks for micro- and nanofluidic systems[6–8]. The wetting and spreading of droplets on complex substrates is governed by surface interactions, interfacial tension and capillarity. The driving mechanisms have been extensively studied on flat homogeneous and patterned substrates[9], going back to Young's work on liquid bridges between flat plates[10]. Although considerable progress has been made[9], a complete theoretical description of wetting transitions remains challenging due to the inherent multiscale nature of the contact line. On real substrates, contact angle hysteresis due to surface roughness or chemical heterogeneity further complicates the understanding even for flat surfaces. Recent advances include, for example, the study of wetting phenomena in triangular grooves[11,12] and wedge geometries[13].

The configuration of a liquid droplet adsorbed to a surface is characterized by the contact line, i.e., the boundary between the wetted and unwetted regions of the surface. On a homogeneous flat surface, a droplet will assume a spherical cap shape with a radius determined by the contact angle and the line tension. The situation is more complicated on complex surfaces and continues to attract theoretical and experimental studies of various geometries including cylindrical fibers[3,14–20], ribbon-like fibers[21,22], and spherical beads[23–25]. Droplets on fibers can assume equilibrium shapes that cannot be realized on planar substrates. The shape is in general not axisymmetric and cannot be described by a single curvature radius. Hence, unlike on a planar surface, a vanishing contact angle is not a sufficient condition for spreading. A droplet on a single fiber can assume two distinct equilibrium shapes: a barrel shape if the droplet volume normalized by fiber radius is large or the contact angle is low, and a clam-shell shape if the droplet size is small or the contact angle is high[26,27]. McHale and Newton[28] have used analytical and finite element calculations to determine the surface free energies of droplet configurations and found that for large droplet volume or small contact angle, the barrel shape is energetically preferred while for small droplet volume or large contact angle, the clam-shell shape has a lower energy. Their results suggest that the stable barrel shape droplets are characterized by an inflection angle where the curvature radius changes its sign. While both curvature radii remain positive at the apex, at the contact line one curvature radius changes sign to reduce the excess Laplace pressure. However, the absolute stability of barrel-shaped droplets is

[a] Department of Materials Science and Engineering, Clemson University, Clemson, SC 29634, USA

* E-mail: uschill@clemson.edu

† Electronic Supplementary Information (ESI) available: Simulation movies of spreading droplets, retracting columns, and morphological transitions are provided as supplementary files. See DOI: 00.0000/00000000. The data and code used to generate the figures in this manuscript can be freely accessed and executed through Code Ocean. See DOI: 00.0000/00000000

ultimately still an open question as the accuracy of the energy obtained from finite element calculations depends on resolution making it difficult to precisely ascertain the region where barrel-shapes have lower energy than clam-shells, as noted by McHale and Newton[28].

Fiber materials consist of many fibers and a liquid droplet can be in contact with two or more fibers simultaneously leading to competing surface interactions. A proto-model for the spreading of droplets attached to multiple fibers is a parallel pair of cylinders forming a "fiber rail". For this arrangement it has been observed that, if the spacing between the fibers is sufficiently small, a droplet of wetting liquid will spontaneously spread out in the inter-fiber space to form a liquid column of constant cross-section[29]. This wicking transition is reversible, i.e., if the fiber spacing is increased above a threshold, the liquid column will retract into a droplet bridge. The first analytical description of the shape of a liquid bridge between two parallel fibers with a small spacing was given by Princen[30], who determined the existence region of the column as a function of fiber distance. Similar to the case of a single fiber, however, the regions of stability of different liquid configurations described by Princen's equation remain unspecified.

Keis et al.[6] have experimentally investigated the spontaneous spreading or retraction of droplets on fiber rails. They determined the critical inter-fiber distance by a dynamic method and found that the wicking kinetics can be described by the Bosanquet law[31] at very short times and the Lucas-Washburn law[32,33] at later times. Protiere et al.[19] conducted experiments with parallel fibers of varying fiber distance and radius, liquid volume, and contact angle, and studied the transition between a hemispherical drop shape and a liquid column. They found that the transition depends on the geometry as well as the liquid volume, and observed a region where both the barrel drop and the liquid column are stable. This suggests that the transition from one morphology to the other exhibits hysteresis. By comparing the surface energy of a column to that of a spherical droplet, a curve above which the droplet energy is smaller than the column energy can be found for each volume. This curve estimates the boundary of the region with stable droplets and it was found to be close to the drop-to-column transition observed in experiments. Protiere et al. hypothesized that the hysteresis is unrelated to contact line pinning or elastic effects, however, the simple energetic model cannot explain the origin of the hysteretic behavior or the size of the hysteresis loop.

Several authors have presented numerical simulations of the 3D shape of liquid bridges between two fibers to predict the capillary forces as a function of fiber distance[17,20,34,35]. Virozub et al. employed the Surface Evolver package to minimize numerically the surface free energy per unit length of the liquid configuration. They used an analytical expression to calculate the resultant forces, energies, and torques exerted by the liquid bridge on the fibers. The results suggest that stable symmetric bridges are favored at small fiber distance, whereas larger contact angles lead to coexistence of stable asymmetric and unstable symmetric configurations. The region of stability and transitions between the shapes were not further discussed. Aziz and Tafreshi[20] reported experiments and numerical calculations of the mechanical forces between two fibers connected by a liquid bridge. The dependence of the force on fiber spacing was studied for parallel and orthogonal fiber configurations, and the detachment force of a pendant bridge was determined as a function of liquid volume. The numerical simulations always started with a cuboid-shaped droplet and the column to droplet transition was thus not observed in this setup. Wu et al.[17] and Bedarkar et al.[35] extended the surface energy formulation by McHale and coworkers to the case fiber rails and also employed the Surface Evolver package to investigate the wetting morphology of droplet for varying liquid volume, fiber spacing, and contact angle. The results indicate that the dependence of the wetting length on the contact angle is strongly affected by the liquid morphology. Wu at al.[17] considered an additional bridge state, where the droplet shape does not engulf the fibers but only partially wraps the outside surfaces. The critical droplet volume where the surface energy of an engulfing barrel shape and the partially wrapping droplet bridge are equal were determined using Surface Evolver. The numerical minimization of the surface energy allows to express the critical condition for absolute stability as a family of characteristic wetting curves in the volume-distance parameter space. The partially wrapping bridge state, which can exist for larger fiber distances, is different from the liquid column observed in experiments[6,19]. Therefore, the wetting curves obtained by energy minimization do not necessarily capture the absolute minimum morphology. The transitions between different liquid configurations and the associated hysteresis thus remain incompletely understood.

An alternative to determining the stable liquid configuration by minimization of the surface energy is to consider the corresponding Young-Laplace equation. In a stable configuration, the excess Laplace pressure is constant everywhere across the droplet surface. Such a configuration is metastable if its surface energy is higher than another stable morphology with the same volume. A morphology transition is thus associated with an energy barrier that corresponds to overcoming Laplace pressure. However, since measuring excess pressure for small liquid volumes is challenging, the connection between the surface energy landscape and capillary pressure in the context of morphology transitions has not been investigated in detail in previous works.

To fill this gap, we use multicomponent lattice Boltzmann simulations to investigate the morphology of liquid wetting on a fiber rail. The multicomponent lattice Boltzmann method[36–39] belongs to the class of diffuse interface methods, where the interface between immiscible fluid components has a finite width controlled by the interaction strength between fluid components. The width of the interface introduces a length scale that can take over the role of the slip length, thus implicitly resolving the Huh-Scriven paradox, i.e., the divergence of the dissipation rate that arises from application of the no-slip boundary condition. The diffuse interface width can also be reconciled with the scaling regimes for moving contact lines[40] and connects to the sharp interface description in terms of the Cox-Voinov relation[41]. Within the LBM, The interfacial tension between the fluids and the contact angle of the three-phase line can be controlled by tuning the interaction parameters between different fluid species and the surface[42]. Ap-

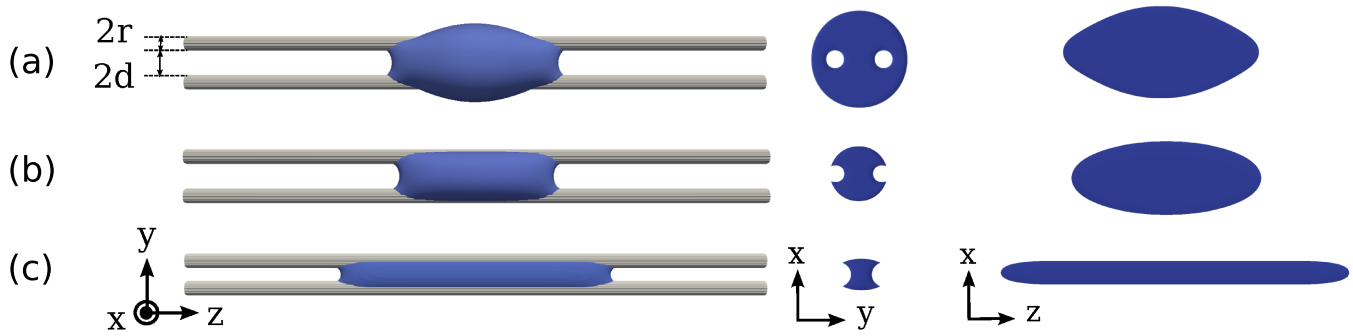


**Fig. 1** Schematic illustration of different equilibrium shapes of liquid droplets on fiber rails. A top view is shown on the left, while the side and cross-sectional views are shown on the right. (a) A barrel shaped droplet fully engulfs the fibers in liquid. (b) A droplet bridge wraps partially around the fibers and forms contact lines on the surface of the fibers. The height and the cross-sectional area of the droplet bridge can vary along the wetting length. (c) A liquid column is similar to the droplet bridge with a constant height and cross-sectional area.

parent phenomena such as contact angle hysteresis and surface slip can in principle be incorporated by explicitly modeling rough or patterned surfaces [43]. The method is thus suitable to model the interactions of wetting liquids with homogeneous fiber surfaces. We study the dynamic spreading and retraction of liquid volumes on fiber rails. The simulations confirm the existence of three possible configurations, barrel-shaped droplet, droplet bridge, and liquid column. The wetting length and capillary pressure of the liquid column configuration is validated against theoretical analysis and experimental measurements. Starting from different configurations, we observe spontaneous capillary motion and identify two bistable regions in the morphology diagram. We investigate the transitions from metastable shapes to lower energy configurations by applying an external force to overcome the energy barrier, which allows us to estimate the critical Laplace pressure associated with the energy barrier. Our simulations and analysis advance the understanding of liquid spreading on fibers and can be used to enhance designs of filtration devices or microfluidic systems for manipulation of small amounts of liquids.

The remainder of the manuscript is organized as follows. In section 2, we briefly review the thermodynamics of interfaces and introduce the multicomponent lattice Boltzmann model. We report the analysis of the simulation results in section 3. The conclusions of our work are discussed in section 4.

## 2 Mathematical and numerical methods

### 2.1 Surface morphology

The equilibrium contact angle $\theta$ between a liquid interface and a solid substrate is controlled by three surface tensions, solid-liquid $\gamma_{SL}$, solid-vapor $\gamma_{SV}$, and liquid-vapor $\gamma$, and can be expressed by Young's equation

$$\cos\theta = \frac{\gamma_{SV} - \gamma_{SL}}{\gamma}. \tag{1}$$

The three surface tensions determine the equilibrium spreading coefficient

$$S_{\text{eq}} = \gamma_{SV} - (\gamma_{SL} + \gamma). \tag{2}$$

If $S_{\text{eq}} \geq 0$, the contact angle is zero and the liquid will spread out as a film on the substrate. Conversely, if $S_{\text{eq}} < 0$, the liquid will assume a configuration with a finite contact angle $\theta$. The Laplace excess pressure $\Delta p$ at a point on the interface is given by the Young-Laplace equation

$$\Delta p = \gamma \left( \frac{1}{R_1} + \frac{1}{R_2} \right), \tag{3}$$

where $R_1$ and $R_2$ are the principal curvature radii. In general, $R_1$ and $R_2$ vary across the surface. The surface free energy $E$ can be written in the form

$$E = \gamma \left( A_{LV} - A_{SL} \cos\theta \right), \tag{4}$$

where $A_{LV}$ and $A_{SL}$ are the liquid-vapor and solid-liquid interfacial areas. To determine the equilibrium morphology, the surface energy has to be minimized subject to given constraints such as constant liquid volume and substrate geometry, e.g., fiber surfaces. Explicit solutions are only available for simple situations such as a spherical droplet on a flat surface, an axisymmetric droplet on a fiber [26], or liquid column on a fiber rail [19]. In general, the solutions to the nonlinear problem require numerical procedures.

For the case of two parallel fibers, the geometric parameters include the fiber radius and the inter-fiber distance. In the discussion of our results below, we categorize three possible equilibrium configurations for liquid wetting on fiber rails: a barrel-shaped drop similar (but not axisymmetric) to an unduloid on a single fiber, a droplet bridge that partially wets the outside surfaces of the fibers, and a liquid column with a constant cross section. The three configurations are shown in Fig. 1. To illustrate the distinction between these configurations, the perpendicular and parallel cross sections at the barycenter of the liquid volume are depicted in Fig. 1. The barrel drop fully engulfs the fibers and has an almost circular cross section near the center. The cross section of the droplet bridge and barrel drop vary along the fiber direction which makes it more difficult to describe them analytically. The droplet bridge has a convex cross section while the liquid column

can have both convex and concave perpendicular cross sections. The liquid column is flat in the parallel direction except near the menisci, hence the cross section is nearly constant and one of the principle curvatures vanishes. The previous approaches for describing the shapes mathematically are typically based on the functional relationship between the wetting length and capillary pressure [15,19,30]. While the column morphology has been studied in some detail in theory and experiment, there have been few attempts to determine the wetting length and capillary pressure of barrel shapes and droplet bridges on fiber rails.

## 2.2 Lattice Boltzmann method

The lattice Boltzmann method is a versatile multiscale method for computational fluid dynamics beyond simple Newtonian liquids [44]. Over the last few decades, various methods have emerged that make the LBM applicable to complex fluids including multiphase/multicomponent fluids [36–39]. In contrast to traditional CFD methods, the dynamics of the fluid is described on a kinetic level and the Navier-Stokes equation emerges as the hydrodynamic limit of an asymptotic expansion. The kinetic description offers a way to dial in specific physico-chemical interactions at the mesoscale which enables coupling of different fluid components and molecular solutes. The dynamics of the fluid is described by the lattice Boltzmann equation

$$\begin{aligned} f_i(\vec{x}+h\vec{c}_i,t+h) &= f_i^*(\vec{x},t) \\ f_i^*(\vec{x},t) &= f_i(\vec{x},t) - \sum_j \Lambda_{ij}\left[f_i(\vec{x},t) - f_i^{\mathrm{eq}}(\rho,\vec{u}^*)\right], \end{aligned} \tag{5}$$

where $\vec{x}$ are discrete positions in space on a cubic lattice with lattice spacing $a$, $h$ is a discrete time step, and $\vec{c}_i$ are discrete velocities such that $h\vec{c}_i$ connects lattice sites. The $f_i$ are local populations representing the mass density of fluid associated with velocity $\vec{c}_i$, and the matrix $\Lambda_{ij}$ represents a collision operator that relaxes the populations towards a discrete Maxwell-Boltzmann equilibrium $f_i^{\mathrm{eq}}$. In this work, we employ the three-dimensional D3Q19 lattice that uses 19 velocities connecting nearest and next-nearest neighbors of the cubic lattice. The equilibrium distribution is taken as the third-order expansion

$$\begin{aligned} f_i^{\mathrm{eq}}(\rho,\vec{u}^*) = \rho w_i[1 &+ \frac{\vec{c}_i\cdot\vec{u}^*}{c_s^2} + \frac{(\vec{c}_i\cdot\vec{u}^*)^2}{2c_s^4} - \frac{u^{*2}}{2c_s^2} \\ &+ \frac{(\vec{c}_i\cdot\vec{u}^*)^3}{6c_s^6} - \frac{u^{*2}(\vec{c}_i\cdot\vec{u}^*)}{2c_s^4}], \end{aligned} \tag{6}$$

and the common Bhatnagar-Gross-Krook (BGK) collision operator $\Lambda_{ij} = \delta_{ij}\tau$ with a single relaxation time $\tau$ is used. The method recovers the incompressible Navier-Stokes equation with a kinematic viscosity $\nu = c_s^2(\tau - h/2)$, where $c_s = 1/\sqrt{3}\ a/h$ is the (pseudo-)speed of sound of the lattice. In the implementation used in this work, the hydrodynamic variables are obtained as moments of the *post-collisional* LB populations

$$\rho = \sum_i f_i^*, \tag{7}$$

$$\rho\vec{u} = \sum f_i^*\vec{c}_i. \tag{8}$$

The distinction between $\vec{u}$ and $\vec{u}^*$ is used to accommodate momentum source terms arising from interactions between different fluid components as introduced in the next subsection.

### 2.2.1 Multicomponent lattice Boltzmann

Multiple fluid components can be incorporated in the lattice Boltzmann method by using multiple sets of populations $f_i^\sigma$ where $\sigma$ indexes the components. Following Shan and Chen [36,37], the interactions between different components or phases are modeled by a non-local interaction forces $\vec{F}^\sigma(\vec{x},t)$ given by

$$\vec{F}^\sigma(\vec{x},t) = -\psi^\sigma(\vec{x},t)\sum_{\bar{\sigma}} g_{\sigma\bar{\sigma}}\sum_{\vec{x}'}\psi^{\bar{\sigma}}(\vec{x}',t)(\vec{x}'-\vec{x}), \tag{9}$$

where $g_{\sigma\bar{\sigma}}$ is an interaction coefficient and $\psi^\sigma(\vec{x},t) = \psi(\rho^\sigma(\vec{x},t))$ are the Shan-Chen pseudo-potentials representing an effective mass. The sum over $\vec{x}'$ runs over the neighboring lattice sites that are connected to $\vec{x}$ by a discrete velocity vector $\vec{x}' - \vec{x} = h\vec{c}_i$. The pseudo-potentials are monotonous functions of density that are taken in the form

$$\psi^\sigma(\vec{x},t) = \psi[\rho^\sigma(\vec{x},t)] = \rho_0\left(1 - \exp[-\rho^\sigma(\vec{x},t)/\rho_0]\right) \tag{10}$$

with a reference density $\rho_0$. In the implementation used in this work, the interaction forces are incorporated in the collision operator by shifting the velocity in the equilibrium distribution by

$$\Delta\vec{u}^{\sigma,*}(\vec{x},t) = \tau\frac{\vec{F}^\sigma(\vec{x},t)}{\rho^\sigma(\vec{x},t)}. \tag{11}$$

The post-collisional hydrodynamic velocity is shifted accordingly by

$$\Delta\vec{u}^\sigma(\vec{x},t) = \frac{h}{2}\frac{\vec{F}^\sigma(\vec{x},t)}{\rho^\sigma(\vec{x},t)} \tag{12}$$

consistent with the usual half-step correction for the force. The interaction coefficient $g_{\sigma\sigma'}$ controls the miscibility of the components: a positive value represents repulsive interactions that lead to demixing. The interaction potential implies a non-ideal equation of state of the form [45]

$$\begin{aligned} p(\vec{x}) = \sum_\sigma \rho_\sigma(\vec{x})c_s^2 + \frac{1}{4}\sum_{\sigma,\bar{\sigma}} g_{\sigma\bar{\sigma}}\sum_{x'}[&\psi^\sigma(\vec{x})\psi^{\bar{\sigma}}(\vec{x}') \\ &+ \psi^{\bar{\sigma}}(\vec{x})\psi^\sigma(\vec{x}')](\vec{x}-\vec{x}')^2. \end{aligned} \tag{13}$$

The interfacial tension between the two components, e.g. liquid and vapor, arises from [46]

$$\gamma_{\sigma\bar{\sigma}} = \int (p_n - p_t)ds \tag{14}$$

and can be calibrated to a desired value by adjusting the interaction strength $g_{\sigma\bar{\sigma}}$. It is worth noting that in the conventional Shan-Chen model employed here it is not possible to tune the

surface tension and the density ratio independently[46]. However, this makes it possible to estimate the interfacial tension from the density difference[42]

$$\gamma_{\sigma\bar{\sigma}} = g_{\sigma\bar{\sigma}} \frac{\rho^{\sigma} - \rho^{\bar{\sigma}}}{2}. \tag{15}$$

To describe liquid-solid interactions, it is convenient to treat the solid as a virtual component and introduce a liquid-solid interaction force analogous to the liquid-liquid interactions[42]

$$\vec{F}_s^{\sigma}(\vec{x},t) = -g_{s,\sigma}\psi_{\sigma}(\vec{x},t)\sum_{\vec{x}'}\psi(\rho_s^{\sigma})(\vec{x}'-\vec{x})s(\vec{x}',t), \tag{16}$$

where $s(\vec{x}',t)$ is 1 if $\vec{x}$ is a solid site and 0 if it is a fluid site, $g_{s,\sigma}$ is the interaction strength between fluid component $\sigma$ and the solid wall, and $\rho_s^{\sigma}$ is a virtual fluid density. The liquid-solid interfacial tension can be calibrated by the interaction strength and a density parameter $\Delta\rho$ such that $\rho_s^{\sigma} = \rho^{\sigma} \pm \Delta\rho$, which leads to $\gamma_{s,\sigma} = \pm g_{s,\sigma}\Delta\rho$ and[42,47]

$$\cos\theta = \frac{2(g_{s,\sigma} + g_{s,\bar{\sigma}})\Delta\rho}{g_{\sigma\bar{\sigma}}(\rho^{\sigma} - \rho^{\bar{\sigma}})}. \tag{17}$$

This provides a convenient way to tune the contact angle through the virtual wall density. If the same interaction strength is used for fluid-fluid and fluid-solid interactions $g_{s,\sigma} = g_{s,\bar{\sigma}} = g_{\sigma\bar{\sigma}}$, the estimated contact angle depends only on the density parameter $\Delta\rho$. It was shown in Ref. 48 that the contact angle $\theta$ follows a linear dependence on the parameter $\Delta\rho$. In practice, the contact angle can be calibrated through geometric measurements for a droplet on a flat substrate or in a duct[47].

In addition to the interaction force, mid-link bounce-back boundary conditions are applied to obtain a hydrodynamic no-slip boundary condition for the fluid velocity at the surface. For details on the the pseudo-potential lattice Boltzmann model, we refer the reader to the review by Chen et al.[49].

#### 2.2.2 Simulation setup

We used the parallel lattice Boltzmann code LB3D[50] to perform simulations of liquid droplets on fiber rails. The simulations were performed in rectangular domain of $150 \times 150 \times N_z$ lattice sites with periodic boundary conditions in all directions. The fibers were modeled as rigid cylinders of radius $r = 10a$ with no-slip boundary conditions employed through a standard bounce-back scheme at the surface. The length $N_z$ of the domain in the direction parallel to the fibers was chosen to accommodate the wetting length and ranges from 600 to 1500 lattice sites. We have checked that an increase of the domain size does not change the measured final wetting length and shape of the liquid droplet.

The BGK relaxation time $\tau_{\sigma}$ for both fluids was set to $1h$ such that there is no viscosity contrast between the liquid phases. The Shan-Chen coupling strength $g_{\sigma\bar{\sigma}}$ was set to 0.14 $\rho_0 a^2/h^2$ to obtain the desired phase separation while maintaining numerical stability. This value leads to an interface thickness of around 6 lattice sites. The corresponding surface tension was determined by preliminary simulations of a static droplet in a $150^3$ domain and fitting Laplace's law which yielded $\gamma = 0.1655\ \rho_0 a^3/h^2$. The contact angle was set by tuning the virtual wall density $\rho_s$ and measuring the contact angle of a droplet on a flat surface. The results reported in this work are based on a contact angle $\theta = 0$ for complete wetting. The fiber surfaces are smooth and chemically homogeneous such that there is no contact angle hysteresis.

The main parameters that determine the liquid morphology on fiber rails are the droplet volume $V$ and the inter-fiber distance $d$. We have used two initial conditions for the droplet configuration, a spherical droplet and a column-like droplet. The initial densities of the two fluid components were set to the values determined in the Laplace-test for a spherical droplet. The column-like droplet is taken as a cylindrical column with spherical caps and is placed such that it only wets the inside surfaces of the two fibers. In order to compare the simulation results to experimental measurements and theoretical expressions, we use the fiber radius $r$ to obtain dimensionless variables for the inter-fiber distance $\bar{d} = d/r$, droplet radius $\bar{R} = R/r$ and droplet volume $\bar{V} = V/r^3$. The time scale of the simulations is determined by the viscosity $\nu$ of the LB fluid. We use a viscous/capillary time scale to obtain a dimensionless time $\bar{t} = t\rho\gamma/(\nu r)$. It is worth noting that one could also use an inertial/capillary time scale $\sqrt{\rho R^3/\gamma}$, however, our main focus is on the stable liquid morphologies where the choice of the time scale is of lesser interest.

Since the multicomponent LBM is a diffuse-interface model, the liquid interface spans several lattice sites. We define the position of the interface between two fluid components as the location where the order parameter $\phi = \rho^{\sigma} - \rho^{\bar{\sigma}}$ is zero. When measuring the liquid volume in the final configuration, we observed a slight decrease compared to the volume of the initial droplet. This decrease was always less than 4% and therefore considered negligible. During the simulations, we monitored the Laplace pressure $\Delta p$ and the surface free energy $E$. The Laplace pressure is measured by taking the difference between the fluid pressure Eq. (13) at the center of the liquid drop and the pressure at the boundary of the simulation domain. Since the fluid densities are constant sufficiently far away from the interface, this calculation corresponds to the pressure drop across the diffuse interface. The free energy is calculated based on the liquid-liquid and liquid-surface interfacial areas. The areas are calculated by integrating the lattice data over the $\phi = 0$ isosurface. We used the criteria

$$\begin{aligned} \left|\frac{\Delta p(t) - \Delta p(t-1000h)}{\Delta p(t)}\right| &< 10^{-5} \\ \left|\frac{E(t) - E(t-1000h)}{E(t)}\right| &< 10^{-5} \end{aligned} \tag{18}$$

to determine that the final equilibrium configuration had been reached.

## 3 Simulations of liquid spreading on fiber rails

### 3.1 Spreading of spherical drop

To investigate the wetting behavior and the equilibrium morphology of liquid droplets on fiber rails, we first consider the spreading of an initially spherical droplet deposited on two fibers, as shown in Fig. 2a. We varied the inter-fiber spacing $\overline{d}$ and the droplet volume $\overline{V}$. Inspection of the final shape reveals three possible equi-

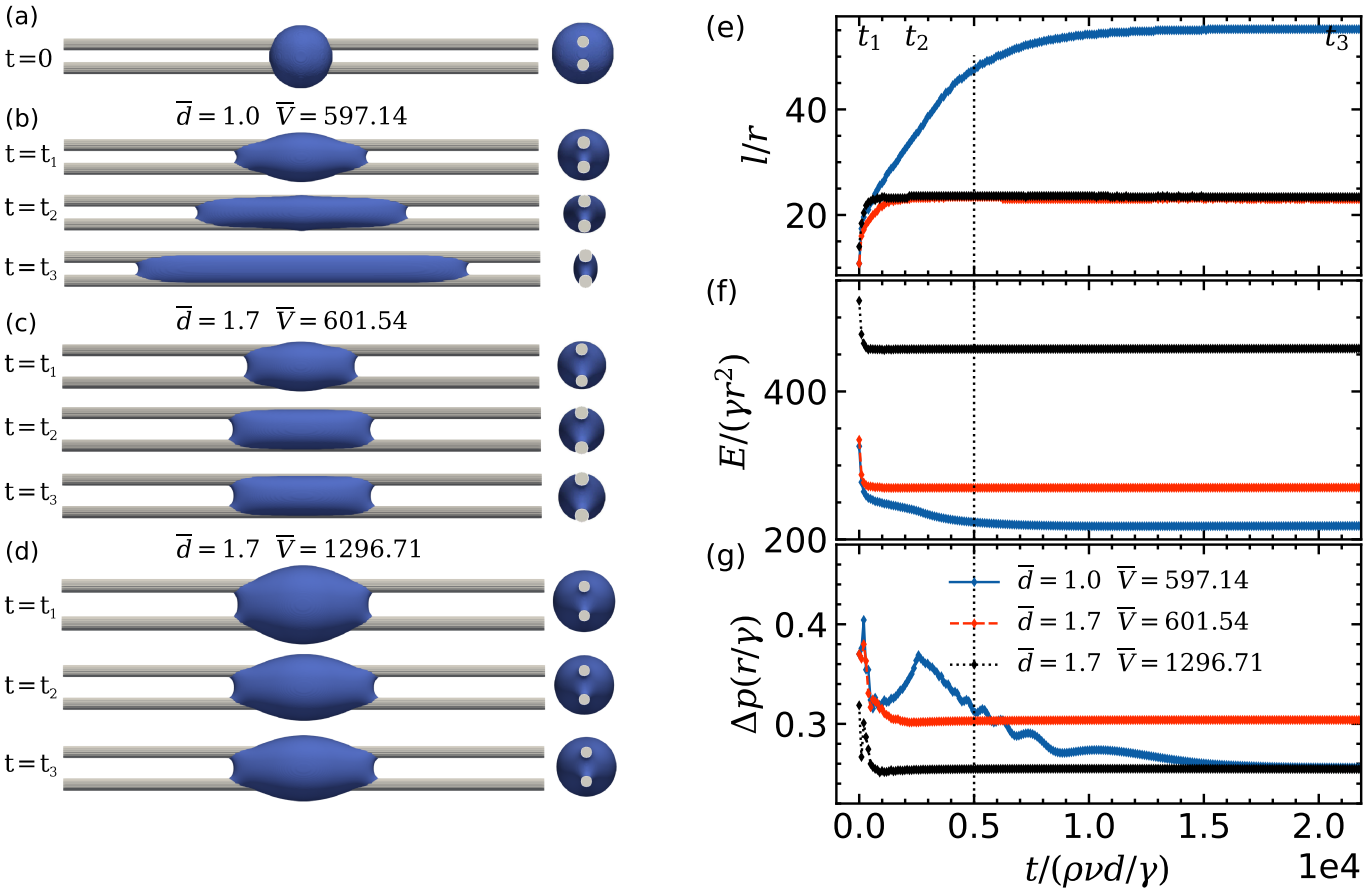


**Fig. 2** Simulation snapshots of the time evolution of a liquid droplet spreading on a fiber rail. (a) The droplet is initialized with a spherical shape. (b) Transition from a barrel droplet to a liquid column. (c) Transition from a barrel droplet to a droplet bridge. (d) Stable barrel droplet. The right panel shows the time evolution of (e) the wetting length, (f) the surface energy, and (g) the Laplace pressure of the droplet.

librium configurations: liquid column, droplet bridge, and barrel-shaped droplets as illustrated in Fig. 2b-d. During the spreading process, the initially spherical configuration morphs quickly into a barrel shape the consecutively continues to spread out on the fiber rail. For the complete wetting case ($\theta = 0$) considered here, the critical fiber spacing beyond which no column configuration exists is $\overline{d}_c = \sqrt{2} \approx 1.41$ [19]. For fiber spacings $\overline{d} = 1.0 < \overline{d}_c$ shown in Fig. 2b, we observe the continuous spreading of the liquid droplet along the fibers, indicated by an increase of the wetting length and a deformation of the cross-sectional shape of the droplet. As $\overline{d}$ increases to 1.7, the liquid does not spread into a liquid column but instead attains a droplet-bridge configuration for smaller volume $\overline{V} = 601.54$, whereas the droplet remains in a barrel-shape configuration for larger volume $\overline{V} = 1296.71$.

The time evolution of the wetting length, surface energy and Laplace pressure calculated from the simulation snapshots is shown in Fig. 2e-f. Fig.2e shows the increase of wetting length in the direction parallel to fiber rails. The capillary motion of liquid droplet comes to rest when the Laplace pressure across the curved interface is constant everywhere. The decay of the surface energy and excess pressure is continuous for the cases that reach a droplet bridge or a barrel shape as the final configuration. The surface energy of the barrel shape is higher than that of the droplet bridge due to the larger liquid interface $A_{LV}$. For the cases that reach a liquid column as the final configuration, we observe noted increase of excess pressure following the initial decay. This is accompanied by a decrease of the principal curvature in the direction perpendicular to the fiber orientation axis, as illustrated by the cross-sections in the side view. Inspection of the cross-sections over time reveals that at time $t = t_2$, the cross section is circular and tangent to the two fibers, while the interface in the parallel direction is nearly flat in the center. Based on these observations, the peak Laplace pressure can be estimated as $\Delta p = \gamma/(d + 2r)$. We conclude that the peak pressure corresponds to a disjoining pressure required to detach the liquid interface from the outside of the fibers such that it can form a contact line on the fiber surface leading to the final column configuration. Following time $t = t_2$, the excess pressure shows slight oscillations that are associated with the decay of capillary surface waves resulting from the detachment of the interface. The surface energy continues to decrease monotonically and reaches the stationary value sooner than the excess pressure. This suggests that the pressure oscillations are in fact a transient effect resulting from the liquid motion. Since here we are primarily interested in the stability of the final configuration, we have not investigated these oscillations further.

### 3.2 Retraction of liquid column

To account for the possibility of metastable configurations, we next consider the retraction of a liquid column. The initial configuration is a cylindrical column of liquid placed between the fibers as shown in Fig. 3a. The liquid volume of the column matches the droplet volume used in the previous section. We varied the inter-fiber spacing $\overline{d}$ and liquid volume $\overline{V}$ over the same range. Inspection of the final interfacial morphology reveals that the same types of equilibrium shapes can be reached, as illustrated in Fig. 3b-d. During the retraction process, we initially observe a rapid deformation of the menisci at the end of the columns driven by the excess pressure. This is evident in the variation of the excess pressure during the initial stage as shown in Fig. 3g. Following this initial relaxation, the surface energy and excess pressure (Fig. 3f and g) vary slowly. The surface energy increases slightly as the bulk energy decreases due to the change of the excess pressure across the meniscus. This suggests that a liquid column configuration is reached shortly after the start of the simulation. We do not observe a distinct signature of the transition from column to droplet bridge. The retracting column either reaches a droplet bridge with the interface attached to the outside of the fibers or a barrel shape that completely engulfs the fibers with liquid. For cases that reach a barrel shape configuration, the retraction of the column proceeds slowly until at time $t = t_2$, a barrel drop is formed. We observe that the bridge is formed asymmetrically as shown in Fig. 3d. An asymmetric liquid bridge was also reported by Aziz et al.[20] in both experiments and numerical energy minimization. Since we do not consider gravity forces in our simulations, the observation suggest that the asymmetric shape is energetically favorable at the given spacing and droplet volume. Non-axisymmetric capillary bridges can indeed form when the volume of the liquid is greater than the volume required to form an axisymmetric spherical bridge[25]. The transition from the liquid bridge to the barrel shape thus shows some analogy to the roll-up of a droplet on a single fiber into a clamshell shape[28]. The formation of the barrel shape is evident in the evolution of the wetting length, surface energy and excess pressure, which show a sudden decrease around time $t_2$. The observations suggests that after the initial relaxation to a liquid column, the transition from column configuration to liquid bridge occurs through slow reconfiguration of the contact line and menisci, followed by a quick wrapping of the liquid around the fibers when the barrel droplet forms. The energy associated with the detachment of the contact line from the fibers constitutes an energy barrier that we will probe in section 3.4.

The

### 3.3 Equilibrium morphology

The two different initial conditions allow us to probe whether the equilibrium configuration of the droplet depends on the starting point in configuration space. In experiments[19], two possible behaviors were observed when the fiber distance $\overline{d}$ was varied at a given droplet volume $\overline{V}$. For small volumes, the droplet shape changes reversibly from a barrel droplet to a column configuration. At larger volumes, the behavior becomes hysteretic with two distinct critical distances for the drop-column transition upon increasing the spacing and the column-drop transition upon decreasing the distance. In our simulations, we investigate the behavior for varying droplet volume $\overline{V}$ at a given fiber spacing $\overline{d}$. Using the two different intial conditions described above allows us to probe whether the equilibrium configuration of the droplet depends on the starting point in configuration space and at which combinations of $\overline{d}$ and $\overline{V}$ both a drop and a column configuration

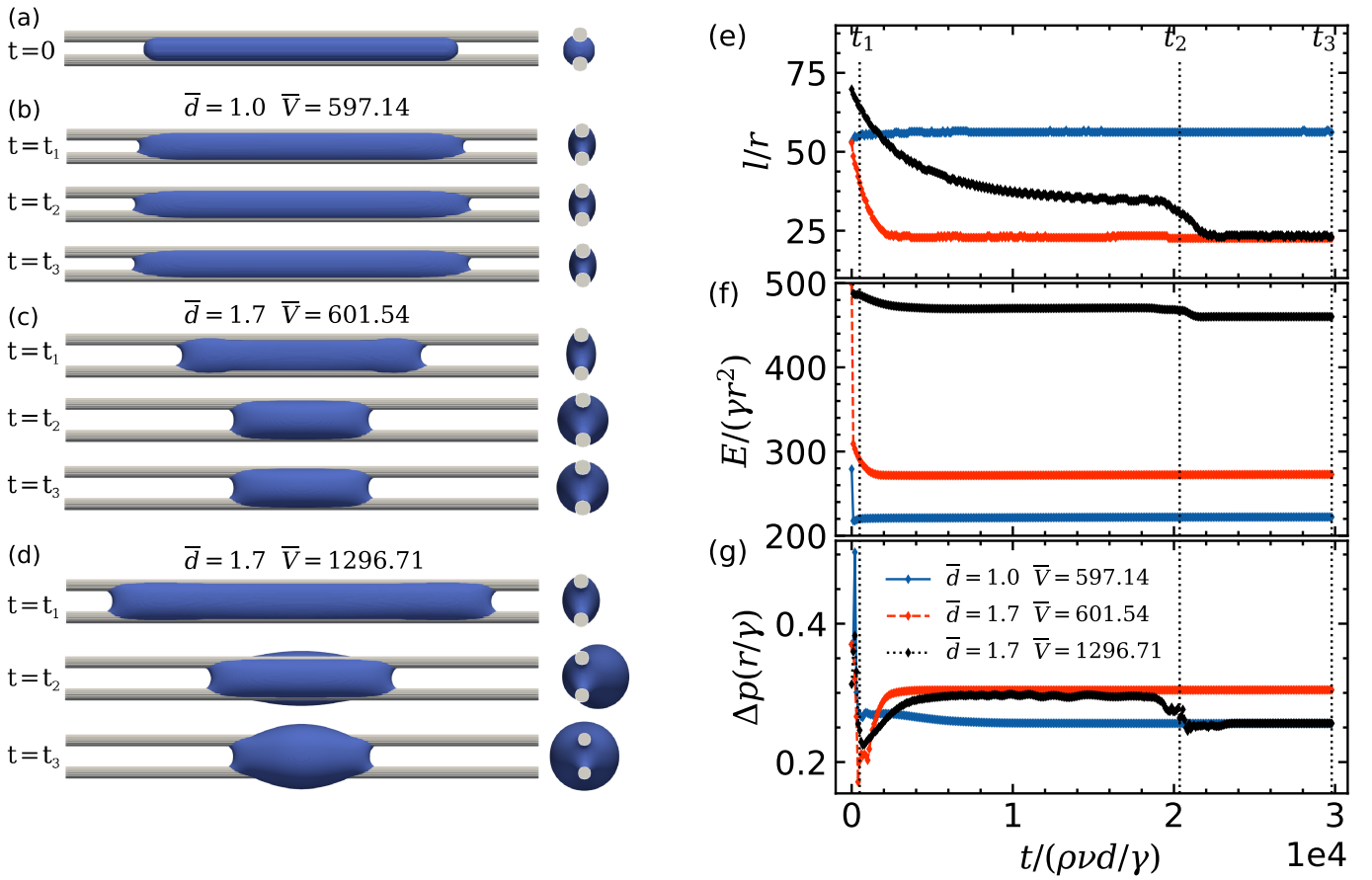


**Fig. 3** Simulation snapshots of the time evolution of a liquid column retracting on a fiber rail. (a) The droplet is initialized with a sphero-cylindrical shape. (b) Stable liquid column. (c) Transition from a liquid column to a droplet bridge. (d) Transition of a liquid column to a barrel-shaped droplet. The right panel shows the time evolution of (e) the wetting length, (f) the surface energy, and (g) the Laplace pressure of the droplet.

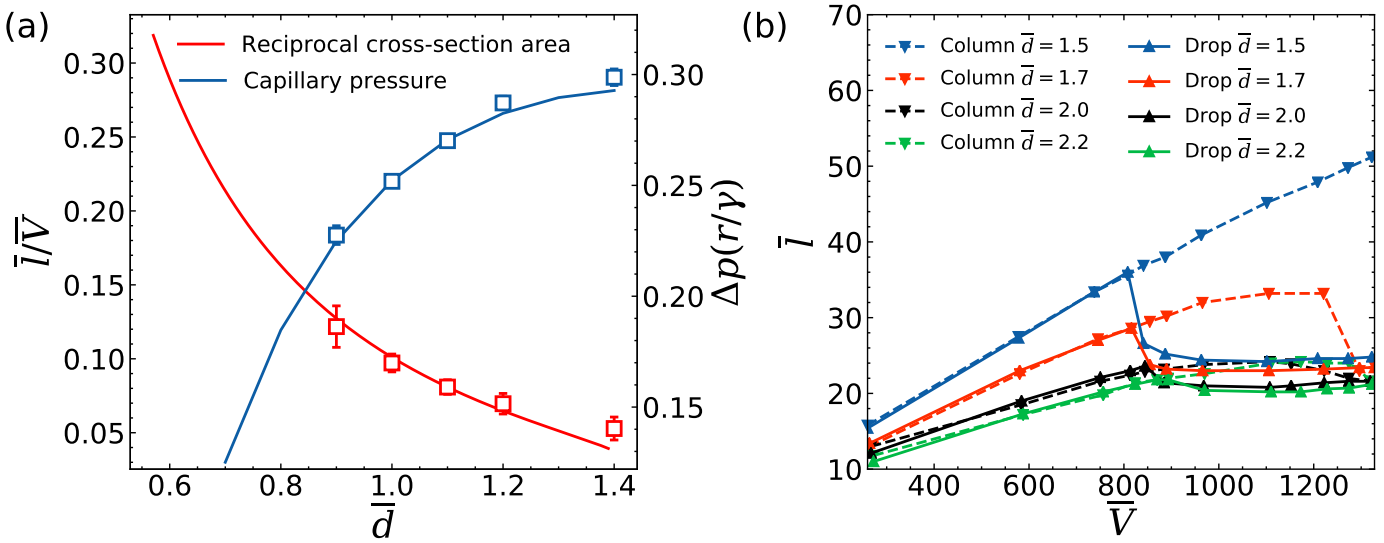


**Fig. 4** (a) The wetting length and the Laplace pressure of the liquid column measured in simulations (symbols) agree with the theoretical prediction (lines). (b) The wetting length of different morphologies measured in simulations as a function of liquid volume for varying inter-fiber spacing. A shape transformation occurs at larger volumes and shows hysteresis between the drop-to-column and column-to-drop transitions.

can exist.

### 3.3.1 Wetting length

Fig. 4a shows the wetting length $\bar{l}$ and equilibrium excess pressure for liquid column configurations as a function of the inter-fiber spacing $\overline{d}$. We report results for inter-fiber spacings $0.9 \leq \overline{d} \leq \sqrt{2} = \overline{d}_c$. For these fiber spacings $\overline{d} > \pi/2 - 1$, the cross section of the liquid column is generally convex. Concave cross sections are indeed observed at lower fiber spacings, however, simulations at lower spacings require increased resolution to exclude inaccuracies in the measurement of the Laplace pressure due to the diffuse interface thickness. The fiber range considered here exhibits the main obsvervations of our study. For the liquid column configuration, the cross-sectional area is constant and the wetting length and equilibrium excess pressure can be calculated analytically[19], cf. appendix A. In Fig. 4 we plot the wetting length and excess pressure calculated from the simulations along with the analytical prediction. The simulation results show excellent agreement with the theoretical values over the range of inter-fiber spacings and liquid volume.

The wetting length of droplet bridge and barrel shape configurations are shown in Fig.4b as a function of the liquid volume $\overline{V}$. At small liquid volumes, both the initialization with a spherical droplet or a liquid column reach a liquid bridge morphology. The wetting length increases with the liquid volume, until the volume becomes sufficiently large to form a barrel droplet with a smaller wetting length. The transitions are clearly visible in the plot and depend on the initial configuration of the liquid. For a given fiber spacing, an initially spherical droplet remains in a droplet-like configuration below a critical volume $\overline{V}_{\mathrm{dc}}$ and spreads into a column configuration above $\overline{V}_{\mathrm{dc}}$ (solid lines in Fig.4b). Conversely, an initial column-like configuration remains in a liquid column above a critical volume $\overline{V}_{\mathrm{cd}}$ and retracts into a droplet-like configuration below $\overline{V}_{\mathrm{cd}}$ (dashed lines in Fig.4b). The column-to-droplet transition occurs at a alrger volume than the droplet-to-column transition, i.e., $\overline{V}_{\mathrm{cd}} > \overline{V}_{\mathrm{dc}}$. A similar hysteretic effect was observed in experiments that varied the fiber spacing at constant volume[19,51]. Both the upper and the lower critical volume show a dependence on the fiber spacing $\overline{d}$. The hysteresis loop becomes larger as the inter-fiber spacing decreases, whereas below $\overline{d} = 1.0$ no hysteresis is observed for the studied drop volume range. We investigate the energy barrier associated with this effect in more detail below.

### 3.3.2 Morphology diagram

The main results for the equilibrium droplet shapes on fiber rails are summarized in the morphology diagram in Fig. 5. The final shapes observed in the simulations over the parameter space $(\overline{d}, \overline{V})$ are indicated by symbols ($\diamond$ for liquid columns, $\circ$ for droplet bridges, $\triangle$ for barrel droplets, and $\star$ for bistable points). A support vector classification (SVC in scikit learn) was used to identify the shaded regions of the morphology diagram. In region (I), only column configurations are found as the final shape of both the spreading droplet and the retracting column. In region (II), only droplet-bridge morphologies are stable. The boundary between regions (I) and (II) is in agreement with the theoretical prediction

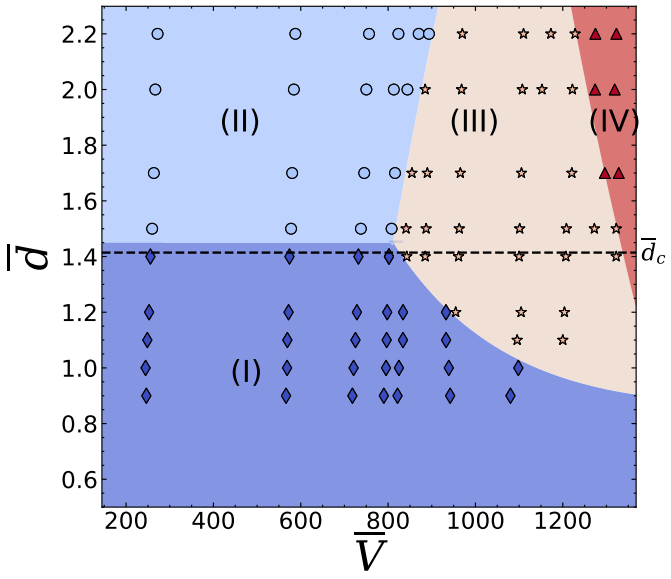


**Fig. 5** Morphology diagram in the parameter space of liquid volume and fiber spacing. The symbols denote the different stable shapes observed in simulations. ($\diamond$) are stable column configurations found in region (I); ($\circ$) are stable droplet bridges found in region (II); ($\triangle$) are stable barrel droplets found in region (IV); the ($\star$) in region (III) denote bistable cases where the final shape depends on the initial configuration. The shaded regions were obtained using a support vector classification trained with the simulation data.

$\overline{d}_c = \sqrt{2}$. In region (IV), only barrel-drop configurations are found as the final morphology. A bistability region (III) is found between the column/bridge and barrel regions, where the final stable morphology depends on the initial configuration. A similar bistable region was reported by Protiere et al.[19] based on experiments. In comparison, we find the boundary between the column and the bistable region at slightly higher volumes V, which is most likely due to the absence of gravity in our simulations. Our simulation results largely agree with previous experimental data and confirm the existence of metastable morphologies for droplets on fiber rails and hysteresis of the morphological transitions. In addition, we find that the bistable region extends beyond the column region to larger fiber spacings $\overline{d} > \overline{d}_c$, where it represents a competition between liquid bridges and barrel-shaped droplets. This transition has not been investigated in detail in experiments due to the difficulty of distinguishing between droplet bridge and barrel shapes. Our simulation results provide an approximation of the boundary of the full bistable region and the critical volumes at which the transitions occur.

### 3.3.3 Bistable region

To investigate in more detail the transitions between liquid column/bridge and barrel-shape configurations, we consider the time evolution of the surface energy and Laplace pressure for varying liquid volume at two different inter-fiber spacings above and below $\overline{d}_c$. The plots in Fig.6 show the wetting length, surface free energy and capillary pressure evolution for spreading and retraction in the bistable and stable regions at $\overline{d} = 1.2$ and 1.7.

Fig. 6a shows a comparison of the drop-to-column and column-

to-drop transitions at $\overline{d} = 1.2 < \overline{d}_c$ for varying values of $\overline{V}$. Below the critical volume, only the liquid column morphology is stable. Hence the equilibrium surface energy and excess pressure are independent of the initial configuration. During the transition from droplet to column the excess pressure passes through a peak followed by slight oscillations, as described before. For a liquid volume $\overline{V} = 1104.55$ in the bistable region, the final morphology is either a droplet or a column depending on the initial configuration. Accordingly, the excess pressure evolution of the initial drop configuration does not display the signature of the drop-to-column transition. The surface energy of the column configuration (solid line) is lower than that of the droplet configuration (dashed line), which indicates that the barrel shapes are metastable and the column morphology is the globally stable configuration.

Fig. 6b shows a comparison of the drop-to-column and column-to-drop transitions at $\overline{d} = 1.7 > \overline{d}_c$. At $\overline{V} = 601.54$ below the lower critical volume, both the spherical drop and the column initialization lead to a liquid bridge with the same surface energy in the final configuration. At $\overline{V} = 1296.71$ above the upper critical volume, both initializations lead to a barrel shape in the final configuration, where the column-to-drop transition shows the signature described before. At $\overline{V} = 1105.37$ in the bistable region, the spherical drop leads to a final barrel-shape while the column leads to final liquid bridge. The surface energy of the barrel drop is slightly lower than the liquid bridge, indicating that in the bistable region above $\overline{d}_c$, the liquid bridge is metastable and the barrel-shape is the globally stable configuration.

It is worth noting that the results are reported here for the complete wetting case ($\theta = 0$) and it can be expected that the contact angle will affect the boundaries between different regions and the size of the bistable region. For instance, the analytical treatment of the liquid column by Princen[30], cf. appendix A, indicates that the critical fiber spacing for the drop-to-column transition decreases with increasing contact angle. Experiments conducted by Sauret et al.[51] suggest that for a partially wetting liquid, the bistable region becomes larger as a larger contact angle hinders the spreading of the liquid thereby increasing the hysteretic effect.

Experiments further suggest that within the bistable region, the effect of gravity may play a role as the Bond number $Bo = \rho g d/\gamma$ is generally larger than unity in this region. The gravity force can prevent the spreading of the liquid into the column configuration thus stabilizing the barrel drop configuration. Preliminary simulations for finite contact angle and with gravity forces seem to confirm the experimental observations. However, comprehensive simulations to quantify the effect of contact angle and gravity on the morphology diagram and energy landscape are beyond the scope of the present work.

### 3.4 Driven morphological transitions

The comparison of the surface energy of the different shapes in the bistable region indicates that there is an energy barrier between the droplet-like configurations and the column-like configurations. It is therefore interesting to characterize the energy landscape of the liquid morphology on fiber rails. As we have seen in Fig.4a and b above, the wetting length $\bar{l}$ is an appropriate parameter to distinguish the possible equilibrium shapes. Hence we plot the evolution of the surface energy $E$ over the wetting length $\bar{l}(t)$ in Fig. 7, where the time $t$ becomes a parameter along the curves, and a metastable shape corresponds to an end point with a finite energy difference $E - E_{\min}$. To estimate the energy barriers associated with metastable states, we induce the shape transition by applying an external force to the droplet as illustrated in Fig. 7e. To induce the drop-to-column transition, we applied a constant compressive force of $g = 7\times10^{-5}\ \rho_0 a/h^2$ to the droplet in the direction perpendicular to the plane separating the fibers. Conversely, to induce the column-to-drop transition, we applied a tensile force of $g = 2\times10^{-4}\ \rho_0 a/h^2$ to the liquid bridge. This force is applied temporarily to increase the free energy until the shape starts to relax spontaneously into a different configuration.

Fig. 7a shows the surface energy at $\overline{d} = 1.2 < \overline{d}_c$ in the column region for three different liquid volumes. In this region the liquid column configuration is the absolute stable shape. For the two lower volumes, the initial droplet transitions spontaneously to the column configuration with a unique equilibrium wetting length. As noted above, the surface energy increases slightly during this process which is offset by the pressure contribution to the bulk energy. For the larger volume, the initial droplet reaches a metastable barrel-shape with a smaller wetting length than the equilibrium column configuration. The metastable state can be driven across the energy barrier as indicated by the dotted line such that it reaches the stable column configuration at a larger wetting length. The energy barrier is small compared to the energy difference between the barrel shape and the column configuration.

The energy landscape for $\overline{d} = 1.7 > \overline{d}_c$ in the droplet region is shown in Fig. 7b for three different liquid volumes. Outside the bistable region, both the spherical droplet and the column initial configurations transition spontaneously to the stable droplet bridge or barrel shape morphology with a unique equilibrium wetting length. For the liquid volume $\overline{V} = 1105.37$ in the bistable region, the initial column maintains reaches a droplet bridge configuration. It can be driven across the energy barrier by a tensile force that stretches the bridge into a bulge (cf. Fig. 7e) that can then transition into a droplet configuration. Although the energy difference between the droplet bridge and barrel droplet configurations is small in this case, the energy barrier indicated by the dotted line in the figure is larger than the barrier for the drop-to-column transition. This energy barrier is associated with the bulge-like deformation of the droplet that is required to detach the contact line from the outside surfaces of the fibers. The difference in the energy barriers together with the smaller region of stability for the barrel-shape configuration suggests that column configurations are easier to observe in experiments. The analysis of the lattice Boltzmann results can thus provide insights into the dynamical evolution of the surface energy during spreading and retraction of droplets on fiber rails that can not be obtained with conventional energy minimization techniques.

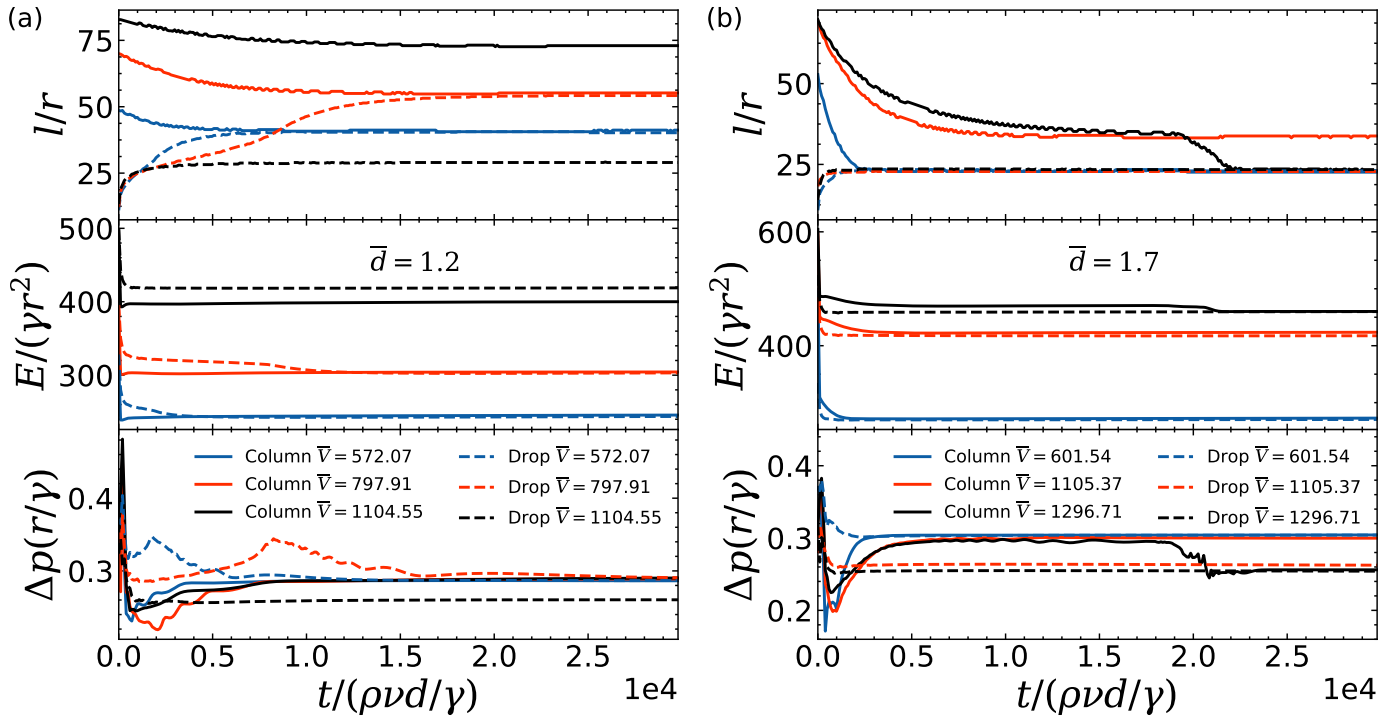


**Fig. 6** Comparison of the time evolution of the wetting length, surface energy, and Laplace pressure for spreading droplets (dashed lines) and retracting columns (solid lines). (a) At a fiber spacing below the critical value, the intermediate peak in the Laplace pressure is a signature of the drop-to-column transition. (b) At a fiber spacing above the critical value, the column configuration is unstable and transitions into droplet bridges at low volume or barrel shapes at high volume. In the bistable region both barrel shapes and liquid bridges can exist.

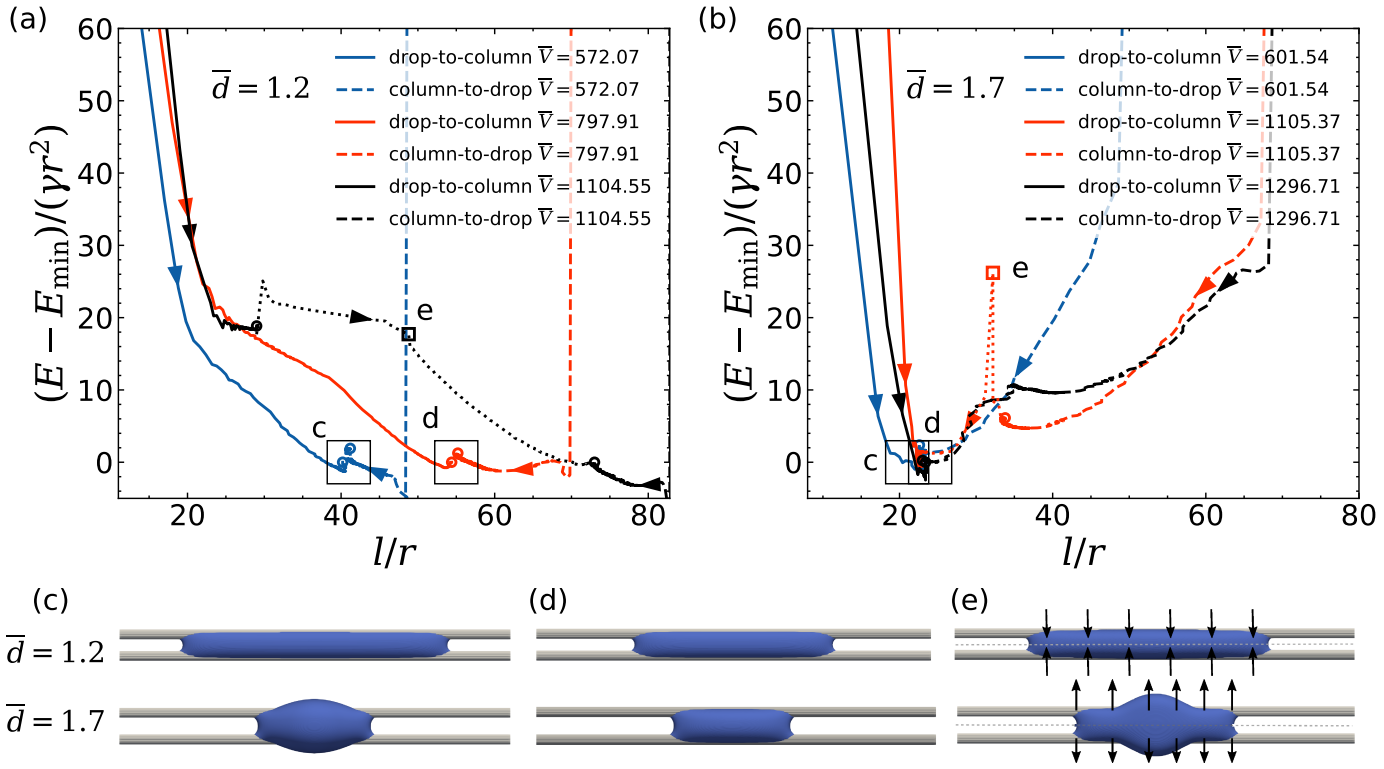


**Fig. 7** Tracking the surface energy during spreading and retraction leads to an approximate energy landscape plotted over the wetting length. Drop-to-column transitions proceed along the curves from left to right, while column-to-drop transitions proceed from right to left. For the configurations marked c and d, the final morphology is the same for both the spreading droplet and the retracting column. Metastable configurations can be driven to a transition by applying an external compressive or tensile force to the droplet (dotted lines). The force is applied until point (e) where the shape begins to relax spontaneously to the globally stable morphology.

## 4 Conclusions

We have studied the morphology of liquid droplets on fiber rails using lattice Boltzmann simulations and compared the results to semi-analytical model calculations. We simulated both the spreading of an initially spherical droplet and the retraction of an initial liquid column at various volumes and inter-fiber spacings. The simulations revealed the existence of metastable shapes and hysteresis of the transitions between drop-like and column-like shapes. By analyzing the time evolution of the wetting length, surface energy, and Laplace pressure we identified the metastable and stable configurations in the parameter space. The presented morphology diagram in the fiber-distance/volume parameter space is consistent with reported experimental results[19]. In addition to previous results, we also found a bistable region in the droplet regime beyond the critical inter-fiber spacing $\overline{d}_c = \sqrt{2}$. This new bistable region corresponds to transitions between droplet-bridges and barrel-shaped droplets. We have introduced a simulation protocol that allows to probe the energy barrier and constructed an energy landscape by tracking the morphology transitions in terms of the wetting length.

Our results provide a quantitative analysis of the shape transitions of liquid droplets on fiber rails. The insights can be used to design enhanced fiber materials for filtration and separation of liquids. For instance, hierarchical porous fibers with a multiscale pore structure could be developed to enhance wicking of liquid into small pores while avoiding clogging of the large-scale pore structure. The general principles of morphological transitions and hysteresis may also find applications in soft robotics. For example, the knowledge of the forces/energies required to induce shape transformations can be used to develop fiber-based manipulators for liquid volumes at small scale.

## Author contributions

Fang Wang: Investigation, Data curation, Visualization, Writing - original draft
Ulf D. Schiller: Conceptualization, Methodology, Formal Analysis, Writing - original draft, Writing - review & editing

## Conflicts of interest

There are no conflicts to declare.

## Acknowledgments

The authors would like to thank Olga Kuksenok and Konstantin G. Kornev for valuable discussions. Clemson University is acknowledged for generous allotment of compute time on Palmetto cluster.

This work was supported in part by the National Science Foundation under NSF Awards #DMR-1944942 and #OIA-1655740. Any opinions, findings and conclusions or recommendations expressed in this material are those of the author(s) and do not necessarily reflect those of the National Science Foundation.

## A Analytical treatment of liquid column

To revisit the analysis of the liquid column[19,30], we consider the geometry shown in Fig. 8. Neglecting the distortion of the cross section near the ends of the column, the wetting length $l = V/A$ can be obtained from the liquid volume $V$, which then allows to calculate the surface energy of the column configuration[30]

$$E_{\mathrm{col}} = \frac{4V}{A}\gamma\left[R\left(\frac{\pi}{2}-\alpha-\theta\right)-\alpha r\right], \tag{19}$$

where the arc lengths of the segments have been expressed through the fiber radius $r$, the radius of curvature $R$, and the angle $\alpha$ between the connecting line of the fibers and the three-phase contact line, cf. Fig 8. For a small increase $\mathrm{d}L$ in wetting length, the surface energy Eq. (4) increases by

$$\mathrm{d}E = \gamma\left[4R\left(\frac{\pi}{2}-\theta-\alpha\right)-4\alpha r\right]\mathrm{d}l, \tag{20}$$

The liquid column is characterized by the Laplace excess pressure

$$\frac{\Delta p}{\gamma} = \frac{1}{R}. \tag{21}$$

By equating $\mathrm{d}E$ to the work done against the excess pressure, we obtain the force balance

$$4\alpha r - 4R\left(\frac{\pi}{2}-\theta-\alpha\right) = \frac{A}{R}, \tag{22}$$

where $A$ is the cross-sectional area. The area $A$ can be expressed in terms of the angle $\alpha$ and the radius of curvature $R$ through the geometric relation

$$\begin{aligned} A &= 4Rr\sin\alpha\cos(\theta+\alpha) \\ &\quad - 2r^2(\alpha-\sin\alpha\cos\alpha) \\ &\quad - 2R^2\left[(\tfrac{\pi}{2}-\theta-\alpha)-\sin(\theta+\alpha)\cos(\theta+\alpha)\right]. \end{aligned} \tag{23}$$

Another geometric relation exists between $R$, $\alpha$, the fiber radius $r$, and the inter-fiber spacing $2d$

$$R = \frac{r+d-r\cos\alpha}{\cos(\theta+\alpha)} \tag{24}$$

such that for given values of $r$, $d$ and $\theta$, the solution for $\alpha$ can be obtained from the condition

$$\begin{aligned} &R^2\left[(\tfrac{\pi}{2}-\theta-\alpha)+\sin(\theta+\alpha)\cos(\theta+\alpha)\right] \\ &\quad + 2rR\left[\sin\alpha\cos(\theta+\alpha)-\alpha\right] \\ &\quad + r^2(\sin\alpha\cos\alpha-\alpha) = 0. \end{aligned} \tag{25}$$

Eq. (24) shows that as the fiber spacing increases, the radius of curvature decreases and changes sign, corresponding to the surface changing from curved inwards to curved outwards. Eq. (25) also determines the critical inter-fiber spacing $d_c$ beyond which no stable liquid column configuration exists. Ref. 19 discussed the case of zero contact angle $\theta = 0$, where $d_c = \sqrt{2}r$.

If the height of the column varies over the wetting length, the angle $\alpha$ will depend on the coordinate of the pinning point $(x, y)$

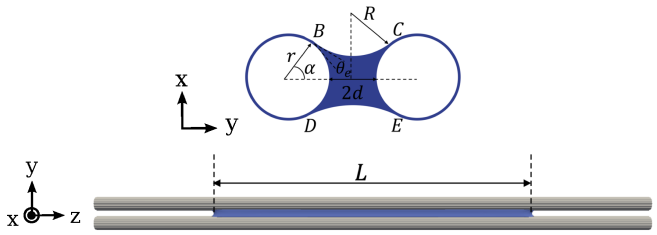


**Fig. 8** Schematic illustration of the cross-sectional geometry of a liquid column between two parallel fibers.

of the contact line $\alpha$

$$y = d + r - r\cos\alpha \tag{26}$$

$$x = r\sin\alpha + R\sin(\alpha+\theta) - R. \tag{27}$$

We assume that the geometry is still described by the curvature radius $R$ of the meniscus in the cross-sectional plane as in Fig. 8. If the shape profile $dz/dy$ of the contact line is known, we can obtain the liquid-fiber and liquid-liquid interfacial areas and the liquid volume by integrating

$$A_{LV} = \int_{\alpha_1}^{\alpha_2} 4R\left(\frac{\pi}{2} - \alpha - \theta\right)\frac{dz}{dy} r\sin\alpha\, d\alpha \tag{28}$$

$$A_{LS} = \int_{\alpha_1}^{\alpha_2} 4r\alpha\frac{dz}{dy} r\sin\alpha\, d\alpha \tag{29}$$

$$V = \int_{\alpha_1}^{\alpha_2} A\frac{dz}{dy} r\sin\alpha\, d\alpha. \tag{30}$$

The surface energy of the circular cross-section region can then be calculated using Eq. (4).

## References


1 R. A. Lodge and B. Bhushan, *J. Appl. Polym. Sci.*, 2006, **102**, 5255–5265.

2 A. M. Rijke and W. A. Jesser, *Wilson J. Ornithol.*, 2010, **122**, 563–568.

3 X. Chen, K. G. Kornev, Y. K. Kamath and A. V. Neimark, *Text. Res. J.*, 2001, **71**, 862–869.

4 P. Contal, J. Simao, D. Thomas, T. Frising, S. Callé, J. C. Appert-Collin and D. Bémer, *J. Aerosol Sci.*, 2004, **35**, 263–278.

5 D. Quéré, *Annu. Rev. Fluid Mech.*, 1999, **31**, 347–384.

6 K. Keis, K. G. Kornev, Y. K. Kamath and A. V. Neimark, *Nano-engineered nanofibrous materials*, 2004, **169**, 175.

7 E. Lorenceau and D. Quéré, *J. Fluid Mech.*, 2004, **510**, 29–45.

8 T. Gilet, D. Terwagne and N. Vandewalle, *Appl. Phys. Lett.*, 2009, **95**, 014106.

9 D. Bonn, J. Eggers, J. Indekeu, J. Meunier and E. Rolley, *Rev. Mod. Phys.*, 2009, **81**, 739–805.

10 T. Young, *Philos. Trans. Roy. Soc. London*, 1805, **95**, 65–87.

11 M. Dokowicz and W. Nowicki, *Langmuir*, 2016, **32**, 7259–7264.

12 M. Dokowicz and W. Nowicki, *Int. J. Heat Mass Transfer*, 2017, **115**, 131–137.

13 E. Ruiz-Gutiérrez and R. Ledesma-Aguilar, *J. Phys.: Condens. Matter*, 2020, **32**, 214007.

14 B. J. Mullins, I. E. Agranovski, R. D. Braddock and C. M. Ho, *J. Colloid Interface Sci.*, 2004, **269**, 449–458.

15 D. Lukáš, J. Chaloupek, E. Košťáková, N. Pan and I. Martinková, *Physica A*, 2006, **371**, 226–248.

16 X.-F. Wu and Y. A. Dzenis, *Acta Mech.*, 2006, **185**, 215–225.

17 X.-F. Wu, A. Bedarkar and K. A. Vaynberg, *J. Colloid Interface Sci.*, 2010, **341**, 326–332.

18 A. Sauret, F. Boulogne, D. Cébron, E. Dressaire and H. A. Stone, *Soft Matter*, 2015, **11**, 4034–4040.

19 S. Protiere, C. Duprat and H. A. Stone, *Soft Matter*, 2013, **9**, 271–276.

20 H. Aziz and H. V. Tafreshi, *Soft Matter*, 2019, **15**, 6967–6977.

21 M. Brinkmann and R. Lipowsky, *J. Appl. Phys.*, 2002, **92**, 4296–4306.

22 C. Zhang and K. G. Kornev, *Surf. Innovations*, 2017, **5**, 194–202.

23 M. Scheel, R. Seemann, M. Brinkmann, M. Di Michiel, A. Sheppard, B. Breidenbach and S. Herminghaus, *Nat. Mater.*, 2008, **7**, 189–193.

24 C. Semprebon, T. Krüger and H. Kusumaatmaja, *Phys. Rev. E*, 2016, **93**, 033305.

25 T. P. Farmer and J. C. Bird, *J. Colloid Interface Sci.*, 2015, **454**, 192–199.

26 B. J. Carroll, *J. Colloid Interface Sci.*, 1976, **57**, 488–495.

27 B. J. Carroll, *Langmuir*, 1986, **2**, 248–250.

28 G. McHale, M. I. Newton and B. J. Carroll, *Oil Gas Sci. Technol.*, 2001, **56**, 47–54.

29 B. Miller, A. B. Coe and P. Ramachandran, *Text. Res. J.*, 1967, **37**, 919–924.

30 H. M. Princen, *J. Colloid Interface Sci.*, 1970, **34**, 171–184.

31 C. H. Bosanquet, *London Edinburgh Dublin Philos. Mag. J. Sci.*, 1923, **45**, 525–531.

32 R. Lucas, *Kolloid Z.*, 1918, **23**, 15–22.

33 E. W. Washburn, *Phys. Rev.*, 1921, **17**, 273–283.

34 A. Virozub, N. Haimovich and S. Brandon, *Langmuir*, 2009, **25**, 12837–12842.

35 A. Bedarkar, X.-F. Wu and A. Vaynberg, *Appl. Surf. Sci.*, 2010, **256**, 7260–7264.

36 X. Shan and H. Chen, *Phys. Rev. E*, 1993, **47**, 1815–1819.

37 X. Shan and H. Chen, *Phys. Rev. E*, 1994, **49**, 2941–2948.

38 M. R. Swift, W. R. Osborn and J. M. Yeomans, *Phys. Rev. Lett.*, 1995, **75**, 830–833.

39 M. R. Swift, E. Orlandini, W. R. Osborn and J. M. Yeomans, *Phys. Rev. E*, 1996, **54**, 5041–5052.

40 H. Kusumaatmaja, E. J. Hemingway and S. M. Fielding, *J. Fluid Mech.*, 2016, **788**, 209–227.

41 R. G. Cox, *J. Fluid Mech.*, 1986, **168**, 169–194.

42 S. Schmieschek and J. Harting, *Commun. Comput. Phys.*, 2011, **9**, 1165–1178.

43 C. Kunert and J. Harting, *Int. J. Comput. Fluid Dyn.*, 2008, **22**, 475–480.

44 S. Succi, *The Lattice Boltzmann Equation: For Complex States of Flowing Matter*, Oxford University Press, 2018.

45 N. González-Segredo, M. Nekovee and P. V. Coveney, *Phys. Rev. E*, 2003, **67**, 046304.

46 M. Sbragaglia, R. Benzi, L. Biferale, S. Succi, K. Sugiyama and F. Toschi, *Phys. Rev. E*, 2007, **75**, 026702.

47 H. Huang, D. T. Thorne, M. G. Schaap and M. C. Sukop, *Phys. Rev. E*, 2007, **76**, 066701.

48 F. Günther, F. Janoschek, S. Frijters and J. Harting, *Comput. Fluids*, 2013, **80**, 184–189.

49 L. Chen, Q. Kang, Y. Mu, Y.-L. He and W.-Q. Tao, *Int. J. Heat Mass Transfer*, 2014, **76**, 210–236.

50 S. Schmieschek, L. Shamardin, S. Frijters, T. Krüger, U. D. Schiller, J. Harting and P. V. Coveney, *Comput. Phys. Commun.*, 2017, **217**, 149–161.

51 A. Sauret, F. Boulogne, B. Soh, E. Dressaire and H. A. Stone, *Eur. Phys. J. E*, 2015, **38**, 62.